NAL TR-974T

ISSN 0389-4010
UDC 621. 438
532. 5

TECHNICAL REPORT OF NATIONAL AEROSPACE LABORATORY

TR-974T

Secondary Flows and Losses in Two Types of Straight Turbine Cascades: Part 1-A Stator Case

Atsumasa YAMAMOTO, Hiroyuki NOUSE

May 1988

NATIONAL AEROSPACE LABORATORY

CHŌFU, TOKYO, JAPAN

Secondary Flows and Losses in Two Types of Straight Turbine Cascades: Part 1-A Stator Case*

Atsumasa YAMAMOTO**, Hiroyuki NOUSE**

ABSTRACT

The present study intends to give some experimental information on secondary flows and on the associated total pressure losses occurring within turbine cascades. Part 1 of the paper describes the mechanism of production and development of the loss caused by secondary flows in a straight stator cascade with a turning angle of about 65 deg. A full representation of superimposed secondary flow vectors and loss contours is given at fourteen serial traverse planes located throughout the cascade. The presentation shows the mechanism clearly. Distributions of static pressures and of the loss on various planes close to blade surfaces and close to an endwall surface are given to show the loss accumulation process over the surfaces of the cascade passage. Variation of mass-averaged flow angle, velocity and loss through the cascade, and evolution of overall loss from upstream to down stream of the cascade are also given. Part 2 of the paper describes the mechanism in a straight rotor cascade with a turning angle of about 102 deg.

概　　要

本論文はタービン翼列内で起こる二次流れとそれに伴って生ずる全圧損失に関する実験的情報を提供することを目的とする。第1部では約65°の転向角を有する直線翼列（静翼列）における全圧損失の発生と発達のメカニズムについて述べる。翼列上流，内部及び下流14断面の一連のトラバース面で二次流れベクトルと損失分布を示す。また，翼表面近傍及び翼端面近傍に沿う種々の面で静圧分布，損失分布を示し，翼列の流路壁面上での損失の移動，蓄積の過程を明らかにする。さらに，質量平均した流れの角度，速度及び損失の翼列を通過する際の変化，翼列の上流から下流へ向かって損失の増加の様子を示す。本論文第2部では約102°の転向角を有する直線翼列（動翼列）についてのメカニズムについて述べる。

NOMENCLATURE

A = control area for calculating mass-averaged value
C_{ax} = cascade axial chord
CP_s = static pressure coefficient based on outlet velocity
CP_t = total pressure loss coefficient based on outlet velocity
$CP_{t,1}$ = total pressure loss coefficient based on inlet velocity
C_{sk} = secondary kinetic energy coefficient = $(V_s/\bar{\bar{V}}_{m,14})^2$
H = blade span
LE = blade leading edge
P_{atm} = atmospheric pressure
P_s = static pressure
P_t = total pressure
TE = blade trailing edge
V_m = resultant flow velocity

* Received March 7, 1988
** Aeroengine Division

V_s = magnitude of secondary flow vector
V_z = axial velocity
Y = spanwise distance from hub endwall
Z = axial distance from blade leading edge
δ_{99} = boundary layer thickness
δ^* = displacement thickness
$= \int_0^{H/2} (1-\bar{V}_m/\bar{V}_{m,\mathrm{mid}})\, dY$
δ^{**} = momentum thickness
$= \int_0^{H/2} (1-\bar{V}_m/\bar{V}_{m,\mathrm{mid}}) \times (\bar{V}_m/\bar{V}_{m,\mathrm{mid}})\, dY$
Δ = interval of contour plot
θ_y = yaw flow angle measured from cascade axial direction
p = density
φ = represents θ_y, V_m, CP_t, V_s, or C_{sk}

Subscripts

1–14 = number of traverse measuring (S3) planes
i = pitchwise number of control areas in one blade pitch
j = spanwise number of control areas in the whole span
mid = midspan

Superscripts

$\bar{}$ = pitchwise mass-averaged value
$\bar{\bar{}}$ = overall mass-averaged value

INTRODUCTION

As reviewed by Sieverding in his recent paper [1], recent progress in basic secondary flow research by many workers has produced a fairly detailed description of the flow mechanisms in turbine blade passages, such as leading edge vortices and their associated three-dimensional separation and reattachment lines. The present author agrees with one of his conclusions, i.e., "It is absolutely essential to know whether each such flow mechanism occurring within the cascade is of only local or of overall significance, since this conditions, to a large extent, the choice of the appropriate endwall flow analysis method". Such knowledge is also important for practical use by desingers in companies and by researchers in the field. This leads to a need for more data to estimate quantitatively the role of each mechanism. Experimental data based on detailed traverse measurements made within various blade rows is especially needed because the real mechanism could be revealed, without the necessity of trying to visualize the mechanism from such results as can be obtained outside the rows. Within the author's knowledge, such complete flow surveys within blade rows have been limited to the following: Langston et al. [2] and Gregory-Smith and Graves [3] for low-speed straight rotor cascades, Sieverding and Wilputte [4] for a high-speed straight stator cascade, and Marchal and Sieverding [5] for both low-speed straight stator and rotor cascades.

In addition to the above straight cascades, Sieverding et al. [6], Boletis et al. [7], Boletis [8], and Yamamoto and Yanagi [9] have presented some detailed traverse data obtained within annular stator cascades.

The present paper intends to give more information on the secondary flow/loss mechanism, based on measurements in two types of turbine cascades with different truning angles.

TEST CASCADE AND TEST CONDITIONS

Low-Speed Straight Turbine Stator Cascade

The blade profile is the same as the mean profile of the first-stage high-pressure turbine stator for aeroengine use [10] and is given in the appendix. The major specifications of the cascade are as follows:

- Blade chord C = 104.4 mm
- Axial blade chord C_{ax} = 81.5 mm
- Blade pitch S = 76.77 mm
- Aspect ratio H/C = 0.96
- Solidity C/S = 1.36
- Number of blades N = 5
- Cascade inlet angle (at design) $\theta_{y,\mathrm{inlet}}$ = 0 deg

- Cascade outlet angle (at design) $\theta_{y,\text{outlet}}$ = −68 deg
- Cascade turning angle (at design) = 68 deg

The cascade is characterized by a large turning angle, thick leading and trailing edges, low aspect ratio and low solidity.

The cascade wind tunnel is of a suction type. It consists of two vertical plates for cascade endwalls, between which a cascade is installed. Two inlet guide plates and two outlet guide plates are set upstream and downstream from the cascade, respectively. A part of one endwall can be moved in the pitchwise direction of the cascade by a pulse motor drive. On the movable wall, there is a radial traverse gear for moving a sensor with a pulse motor drive is set.

The stator blades were made of engineering plastic. Clearance between the movable wall and the blade tip was sealed by felt material (Fig. 1). In the present test of the stator cascade, two sheets of about 5 mm-wide × 0.1 mm-thick aluminium film are attached near two blade tips. (This can be seen in Fig. 1 in Part 2). This was for making electric contact of the sensor with the blade surface in order to stop the present automatic measuring system, when such contact happens during the traverse measurments.

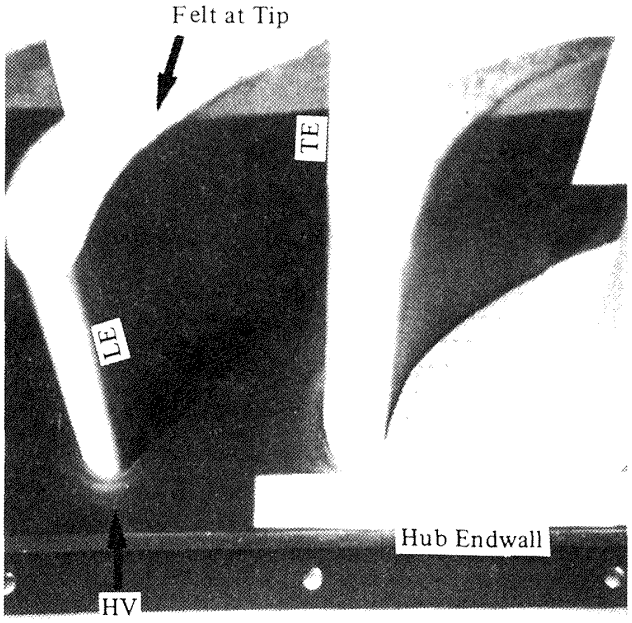

Fig. 1 Test cascade (stator case)

Test Conditions

Fourteen measuring planes analyzed in the paper are shown in Fig. 2. The cascade outlet flow velocity far downstream of the cascade was kept constant for all traverse measurements. For this, a Prandtl-type total/static pressure probe was used. The test Reynolds number, based on the mass-averaged outlet velocity at the furthest downstream traverse plane (plane 14, Z/C_{ax} = 1.28) and the blade chord, was about 2.8×10^5.

Differences between the design and the test flow angles are as follows:

	Design	Test
Inlet flow angle	0 deg	−2.9 deg (i=−2.9 deg at plane 1)
Outlet flow angle	−68 deg	−67.7 deg
Turning angle	68 deg	64.8 deg

The inlet flow conditions and the inlet endwall boundary layer parameters are as follows:

Density ρ = 1.22 kg/m^3
Viscosity ν = 1.44×10^{-5} m^2/s
$\bar{\bar{V}}_{m,1}$ = 13.8 m/s
$\bar{\bar{V}}_{m,1,\text{mid}}$ = 14.2 m/s
$\bar{\bar{V}}_{m,14}$ = 38.3 m/s
Turbulence intensity in free stream $T_{u,1}$ = 0.5 percent

	Hub	Tip
Boundary layer thickness δ_{99}/H	0.180	0.210
Displacement thickness δ^*/H	0.0166	0.0301
Momentum thickness δ^{**}/H	0.0136	0.0181
Shape factor δ^*/δ^{**}	1.22	1.66

The above boundary layer parameters were calculated from the spanwise distribution of the pitchwise mass-averaged resultant velocity at the cascade inlet plane 1 (i.e., Z/C_{ax} = −0.25 in Fig.

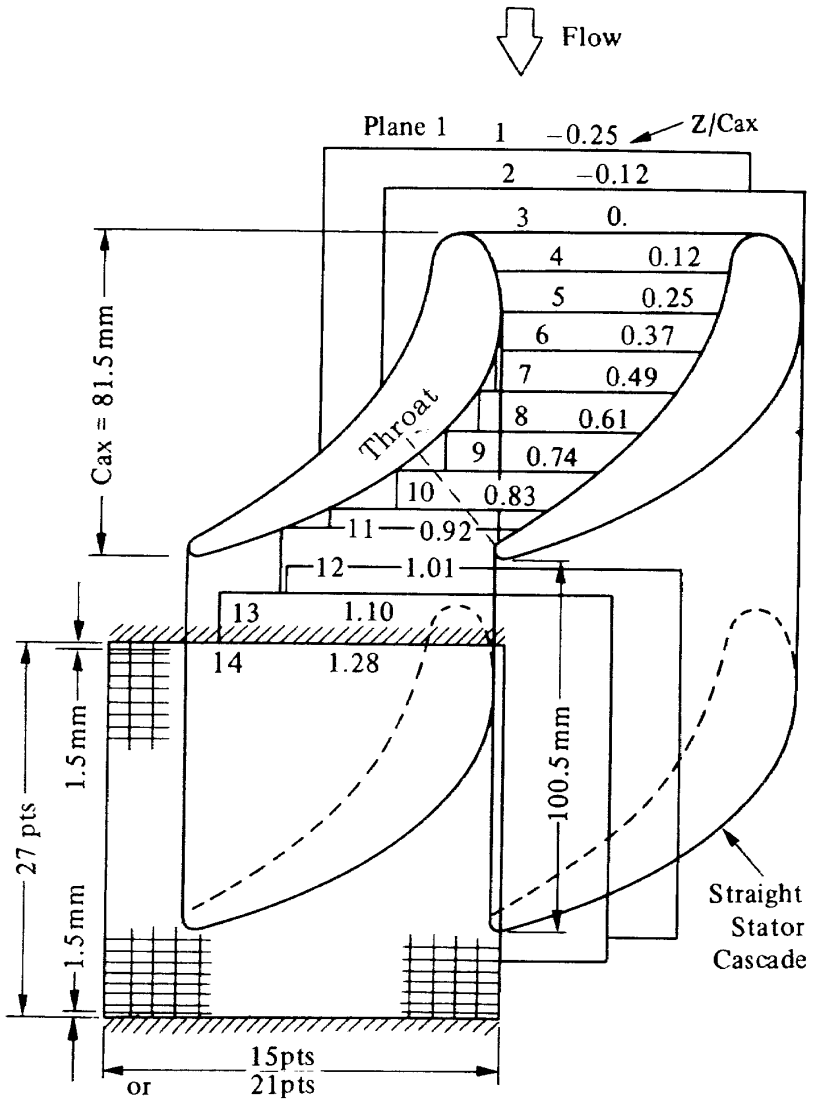

Fig. 2 Traverse measuring planes of straight stator cascade (S3 planes)

6).

The sensor used for traverse measurements was a cobra-type five-hole pitot tube, with a head size of 1.5 mm. All traverse measurements were made under automatic control of a microcomputer. The mechanical resolution of the device was less than 0.01 mm for both spanwise and pitchwise direction of the cascade. All pressures were measured by individual transducers to save the scanning time of the pressures. Yaw direction of the pitot tube was kept in a constant direction during each traverse measurement. Absolute flow directions were then determined by using the pressure data with a calibration map which was programmed on a Vax 11/750 minicomputer.

ANALYSIS METHOD

Definition of Secondary Flow (Deviation from Flow at Midspan)

In the present analysis for straight cascades, the pitchwise local flow directions at the midspan were used to determine the secondary flow vectors at other spans; secondary flow vectors were calculated in a way that flows at other spans were projected onto a plane normal to the flow direction at the midspan which is located at the same pitchwise location as the calculated points.

The secondary flow vectors V_s were normalized by the mass-averaged flow velocity at plane 14, i.e., $\overline{\overline{V}}_{m,14}$ at Z/C_{ax} = 1.28. The normalized

secondary flow vectors were drawn by looking at them from the downstream side of the cascade.

The secondary kinetic energy coefficients C_{sk} is calculated by

$$C_{sk} = (V_s/\bar{\bar{V}}_{m,14})^2 \text{ and } C_{sk,1} = (V_s/\bar{\bar{V}}_{m,1})^2$$

Total and Static Pressure Coefficients (CP_t and CP_s)

Total pressures P_t were normalized in the form of total pressure loss coefficients by

$$CP_t = (P_{atm} - P_t)/(0.5 \times \rho \times \bar{\bar{V}}^2_{m,14})$$

and

$$CP_{t,1} = (P_{atm} - P_t)/(0.5 \times \rho \times \bar{\bar{V}}^2_{m,1})$$

where P_{atm} is the atmospheric pressure and ρ is density. $\bar{\bar{V}}_{m,14}$ and $\bar{\bar{V}}_{m,1}$ are the mass-averaged cascade outlet velocity at plane 14 and the mass-averaged inlet velocity at plane 1, respectively.

Similarly, static pressure P_s is normalized by

$$CP_s = (P_s - P_{atm})/(0.5 \times \rho \times \bar{\bar{V}}^2_{m,14})$$

Pitchwise-Averaged Yaw Flow Angle, Velocity, Total Pressure Loss Coefficient and Overall Loss

The averaging method adopted is that of mass averaging. In each small control area ($A_{i,j}$) formed by four neighboring measuring points, the values at the four points of yaw flow angle ($\theta_{y,i,j}$), resultant velocity ($V_{m,i,j}$), total pressure loss coefficient ($CP_{t,i,j}$), axial velocity ($V_{z,i,j}$) and secondary flow velocity ($V_{s,i,j}$) were arithmatically averaged individually. In the region near the blade surfaces and the endwalls, the values on the surfaces and on the walls (i.e., boundary values) were estimated with a linear extrapolation of experimental data, and the same averaging procedure was applied to each control area in the region by using four values of two measured data and two estimated boundary values. Then, pitchwise mass-averaged values ($\bar{\varphi}$) and overall mass-averaged values ($\bar{\bar{\varphi}}$) were calculated by

$$\bar{\varphi} = \sum_i (\varphi \times A \times V_z)_{i,j} / \sum_i (A \times V_z)_{i,j}$$

and

$$\bar{\bar{\varphi}} = \sum_j \sum_i (\varphi \times A \times V_z)_{i,j} / \sum_j \sum_i (A \times V_z)_{i,j}$$

where φ represents θ_y, V_m, CP_t, V_s, or C_{sk} ($= V_s^2/V_{m,14}{}^2$).

S1, S2 and S3 Planes

Similarly to Wu's definition [11] of surfaces, i.e., S1 and S2 surfaces, for cascade flow analysis, and an additional plane S3 were defined as follows (see also the sketch in Fig. 4): S1 planes are blade-to-blade surfaces parallel to the cascade endwalls: S2 surfaces are meridional surfaces roughly parallel to the blade surfaces; and S3 planes are orthogonal channel surfaces which are parallel to the cascade pitchwise direction. S3 planes correspond exactly to the traverse measuring planes shown in Fig. 2.

Contour plots on an S1 (blade-to-blade) plane and on two S2 planes near both blade surfaces are obtained by using the data on S3 (traverse) planes.

EXPERIMENTAL RESULTS AND DISCUSSION

Secondary Flows and Total Pressure Losses at Traverse Planes (S3 Planes, Fig. 3)

Fig. 3 shows a general view of production and development of secondary flows and the associated losses within the present cascade. Due to the special treatment made near the blade tips, as mentioned previously, and due to a little different boundary layer development on the cascade inlet endwalls, as shown at plane 1 of Figs. 3 and 6, the flow fields are not completely symmetric against the midspan line of the passage. The following discussion will be made mostly on flows at the hub-side half of the passage.

The flows of planes from 3-6 show a weak vortex rotating in the counter-clockwise direction at the suction surface (SS)/hub endwall corner. This vortex (countervortex CV) corrspnds to the suction-side leg of the leading edge horseshoe vortex HV formed on the end-

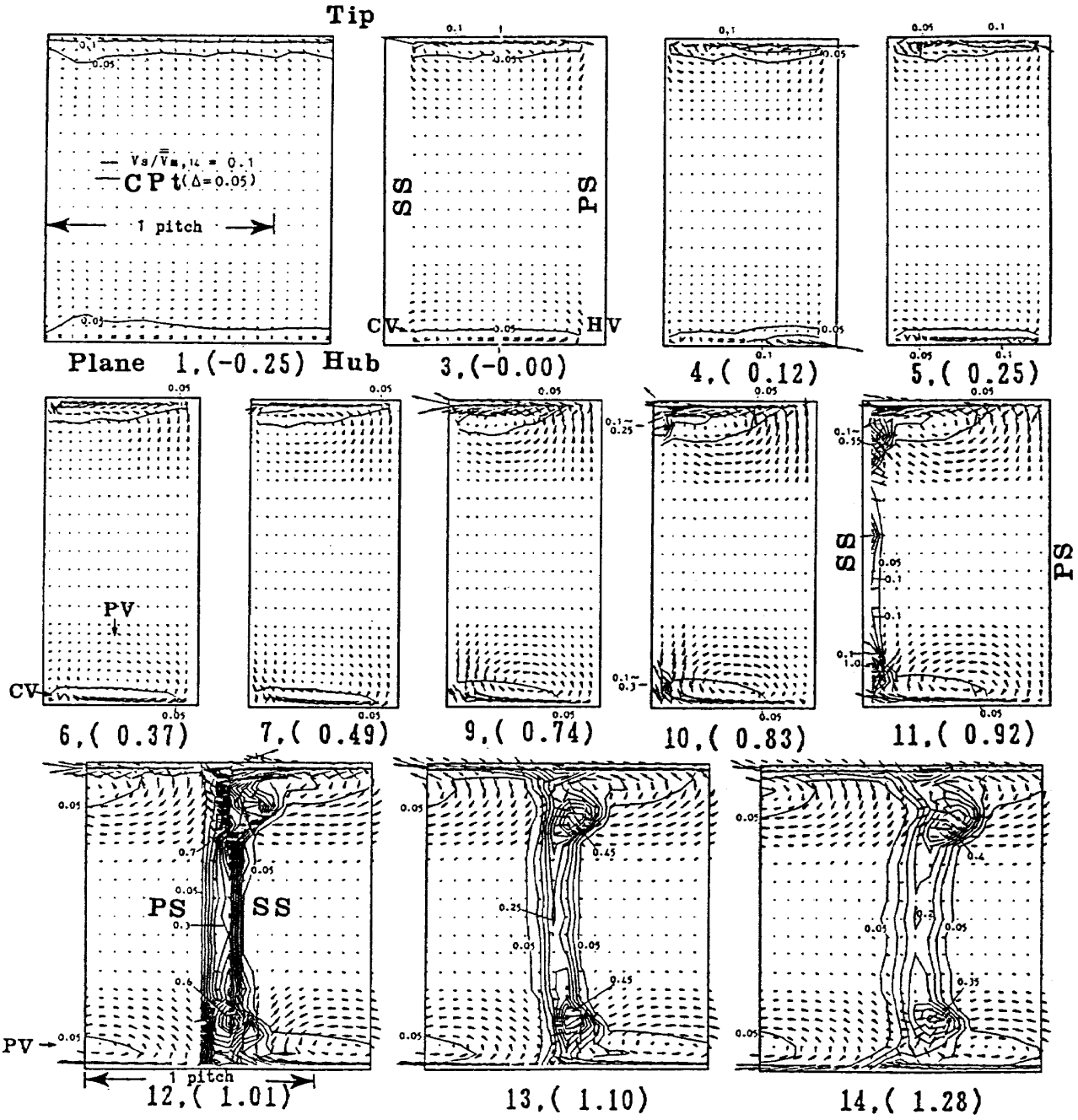

Fig. 3 Development of secondary flows and total pressure losses before, within, and after a straight stator cascade, S3 planes, (Z/C_{ax})

wall. Marchal and Sieverding [5] measured this counter vortex at the upstream inlet plane and at about Z/C_{ax} = 0.15 of their straight stator cascade. The position of the vortex in the present case seems to remain at the corner up to Z/C_{ax} = 0.37, i.e., plane 6. The vortex does not seem to affect loss distribution very much. The votex tends to shift the loss contour toward the endwall. It has almost disappeared at plane 6, while the passage vortex PV becomes clear near the endwall. On the other hand, it was difficult to recognize the pressure-side leg of the horseshoe vortex which should exist near the pressure surface (PS)/endwall corner of the leading edge. The scondary flow vectors at the corner show weak flows moving toward the endwalls along the PS. The flows, then, turn around the endwall corner and pass the endwall from the pressure side to the suction side. The flows finally collide with the countervortex near the SS/endwall

corner.

The endwall (secondary) flows moving toward the suction side at plane 3 change their flow direction to the pressure side on a part of the endwalls at planes 4 and 5. This part of the endwall may correspond to the reverse flow region located at the pressure side of the leading edge. This region can be seen in Langston's flow visualization [2] and in Hah's analysis [12] of endwall boundary layer flows. This would be due to flow separation at the leading-edge/PS corner.

Two passage vortices near both endwalls grow up as they pass further downstream at planes 6-11 within the cascade. The rotational motion of the vortices pushes low-energy fluids of the endwall boundary layers toward the suction side. Similarly to the results obtained by Langston et al. [2], Marchal and Sieverding [5] and Gregory-Smith and Graves [3], the figures at planes 9-11 show that the passage vortices roll up the low-energy fluids onto the SS and that they generate high-loss cores there, while they make the loss region near the pressure surface/endwall corners thinner.

Downstream the cascade at planes 12-14, the strength of rolling-up of the passage vortices increases once in the wake at plane 12 and decreases further downstream. The wake width gets wider and the loss values in the loss cores decreases, due to fluid mixing between the low-energy fluids in the wake and the high-energy fluids outside the wake. This mixing causes additional loss which will be seen later on the mass-averaged overall loss shown in Fig. 7. An experimental analysis on this downstream mixing has recently been given by Moore and Adhye [13], who show that the sum of the mass-averaged total pressure loss coefficient and the kinetic-energy coefficient of secondary flow remains almost constant in their case. This means that the increase of overall CP_t downstream of the cascade results mainly from the decay of the secondary flows.

The regions where the secondary flows dominate are restricted only within about 1/4 span from the endwalls in the present stator cascade with about 65 deg turning, and passage vortices of this rather flat form are similar to those obtained by Gregory-Smith and Graves [3] for a straight rotor cascade with 110 deg turning. It is noteworthy that the distance of the passage vortex center from the endwall is always constant through this stator cascade.

Static Pressure Distribution on S1, S2 and S3 Planes within Stator Cascade (Fig. 4)

The two S1 (blade-to-blade) planes shown in Fig. 4 correspond to the planes located apart from the hub endwall by 1.49 percent and 50 percent of the span height. On the other hand, the two S2 surfaces are not located at constant distances from each blade surface and may be seen as the lines connecting all edges at the SS side or the PS side of the contours on S1 plane in Fig. 4.

Comparison of solid lines and dashed lines on the S1 plane indicates that the blade-to-blade static pressure distribution at the midspan differs from that near the endwall, due to the endwall shear flows. The differences can be found especially in the regions near the PS side of the upstream region and near the SS side of the downstream region within the cascade. Departure of the point of minimum static pressure from the SS was discussed by Langston et al. [2] based on their endwall static pressure data in a straight rotor cascade. The present results on the two S1 planes show that the points are always located apart from the SS not only on the endwall but also at the midspan.

Static pressures over the PS are fairly uniform along the span except near endwall corners, as shown in the result on an S2 plane near the PS. The pressures over the SS, however, are fairly nonuniform, especially near endwalls downstream from the passage throat. This was caused by the two passage vortices.

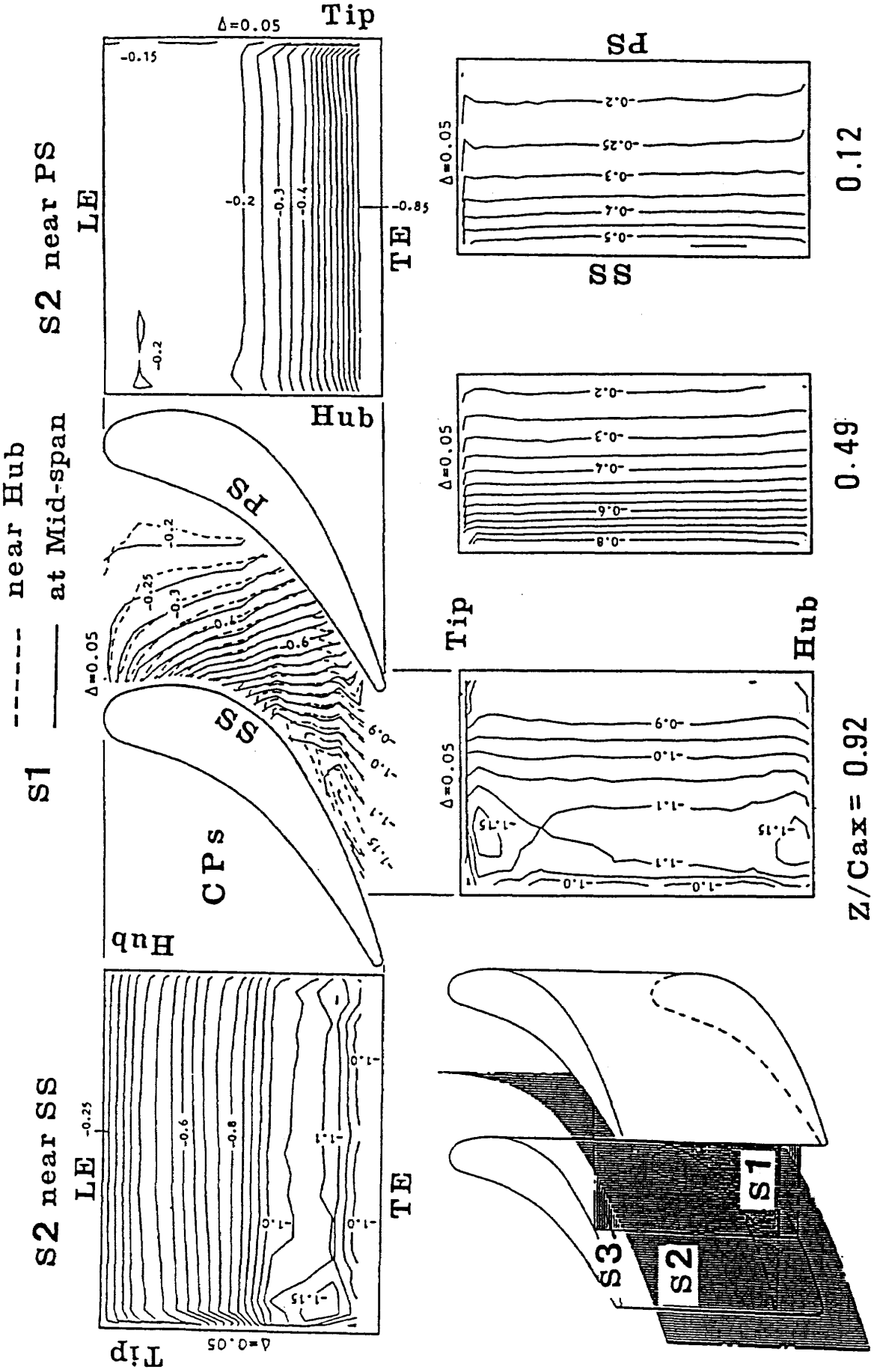

Fig. 4 Static pressure distribution on various planes within a stator cascade

The contours of CP_s at the three S3 planes show the change of the static pressure within the cascade; up to plane 7 (Z/C_{ax} = 0.49), no significant disturbance due to the passage vortices occurred.

Total Pressure Loss Distribution on S1, S2 and S3 Planes within Stator Cascade (Fig. 5)

The loss distribution on the S1 plane near the hub endwall reveals two peaks; one is located at the inlet region and the other is located in the flow deceleration region near the SS just downstream from the throat. The former may be located in the low-energy region along the pressure side separation line(s) shown by Sjolander [14] and by Marchal and Sieverding [5], The latter location corresponds roughly to the minimum pressure point near the endwall, as seen previously. It may be interesting to note that there is a corner region along the SS (indicated by CP_t = 0.06) where CP_t is lower than in the neighboring region. The region extends up to Z/C_{ax} = 0.37 (plane 6). This corresponds to the plane where the suction-side leg of the leading-edge horseshoe vortex almost disappeared.

The loss distribution on the S2 plane near the PS shows that high-loss regions are restricted only to PS/endwall corners near the leading edge. The other distribution on S2 near the SS, however, shows that low-energy fluids gradually cover the surface from the endwall side toward the midspan. Then the low-energy fluids rapidly cover the deceleration flow region downstream of the throat.

The results given at various S3 planes show the migration of endwall low-energy fluids from the pressure side to the suction side. We note especially the movement of the maximum loss values along the walls. Except for the high-loss core on the tip endwall, there exist three local peaks on the SS near the trailing edge, as seen at the S3 plane 11 (Z/C_{ax} = 0.92) and at the S2 plane near the SS. Two of these were produced by the interaction of the passage vortices with the SS near the endwalls. The other, at the midspan, may be produced by the suction surface boundary layer fluids plus some of the low-energy fluids transported from both of the loss cores.

Spanwise Distribution of Pitchwise Mass-Averaged Yaw Angle, Velocity, and Loss Through Stator Cascade (Fig. 6)

Fig. 6 shows, from the yaw angle variation, that the actual turning angle in the present test is about 65 deg. The incidence is −2.9 deg. The yaw angle at plane 4 (Z/C_{ax} = 0.12, just downstream from the cascade inlet plane) shows very large variation close to the endwalls. This was probably caused by endwall separation near the PS, as was seen in Fig. 3. All the yaw angle curves at planes 6-14 show typical shapes of yaw distribution under the effect of secondary flows (passage vortices); i.e., the curves have two underturning parts and two overturning parts near the endwalls compared to the angle at the midspan.

The velocity distribution of Fig. 6 shows fairly large acceleration of the cascade flow and the change of the boundary layer profiles through the cascade. The ratio of acceleration ($\bar{\bar{V}}_{m,14}/\bar{\bar{V}}_{m,1}$) is about 2.78. The inlet boundary layer thickness is about 0.2 of the span height. Effects of the passage vortices on the velocity curves appear especially at planes 11-14; velocity defects at planes 13 and 14 occur at about 0.18 × span height from both endwalls.

CP_t increased rapidly at plane 12 which is located just downstream from the cascade (Z/C_{ax} = 1.01). The value includes the wake loss. Downstream from the cascade (see planes 12-14), the rate of the increase goes down. The local peaks of CP_t at planes 12, 13 and 14 close to the endwalls correspond to the high-loss cores. Apparently they are caused by the passage vortices.

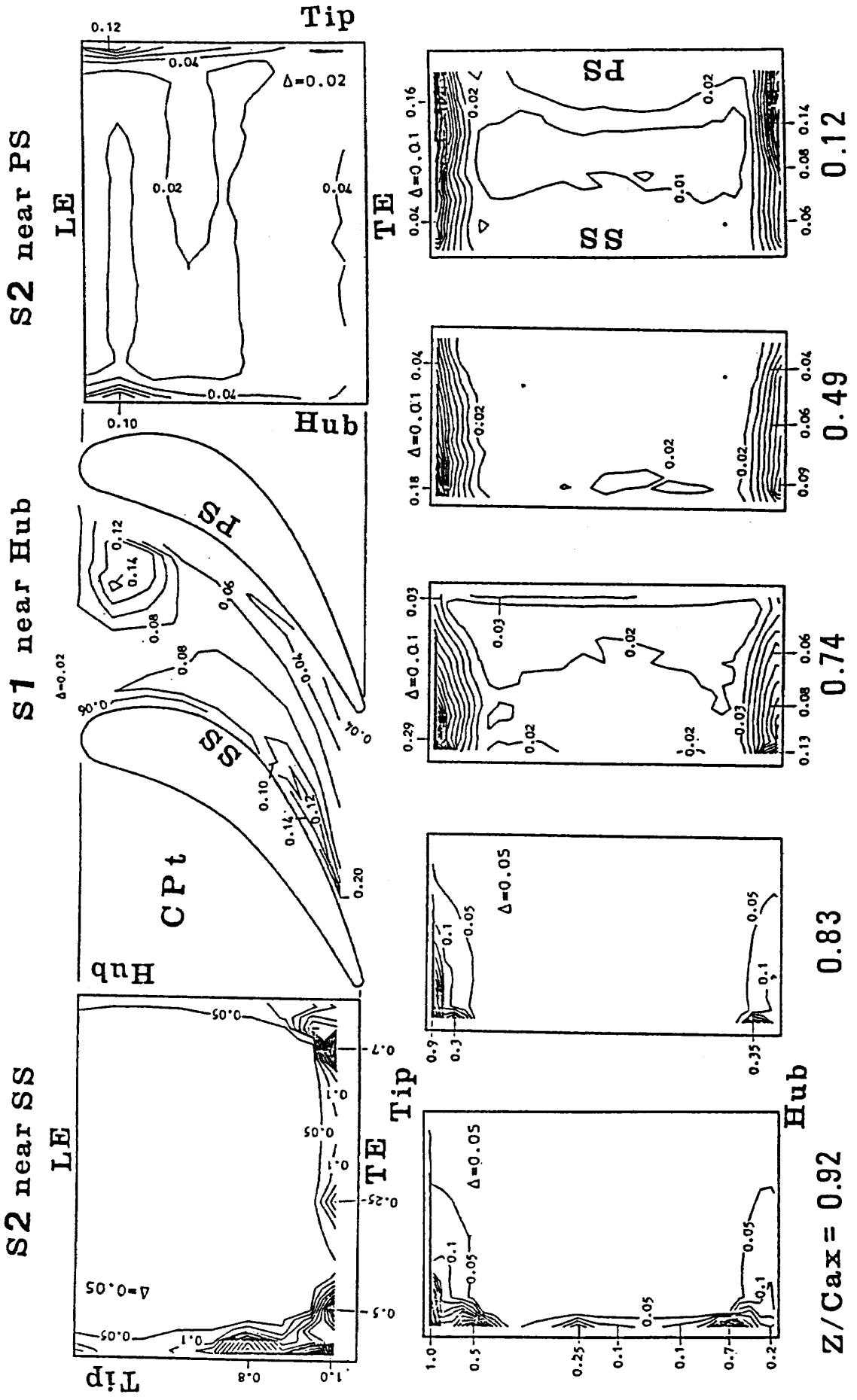

Fig. 5 Total pressure loss distribution on various planes within a stator cascade

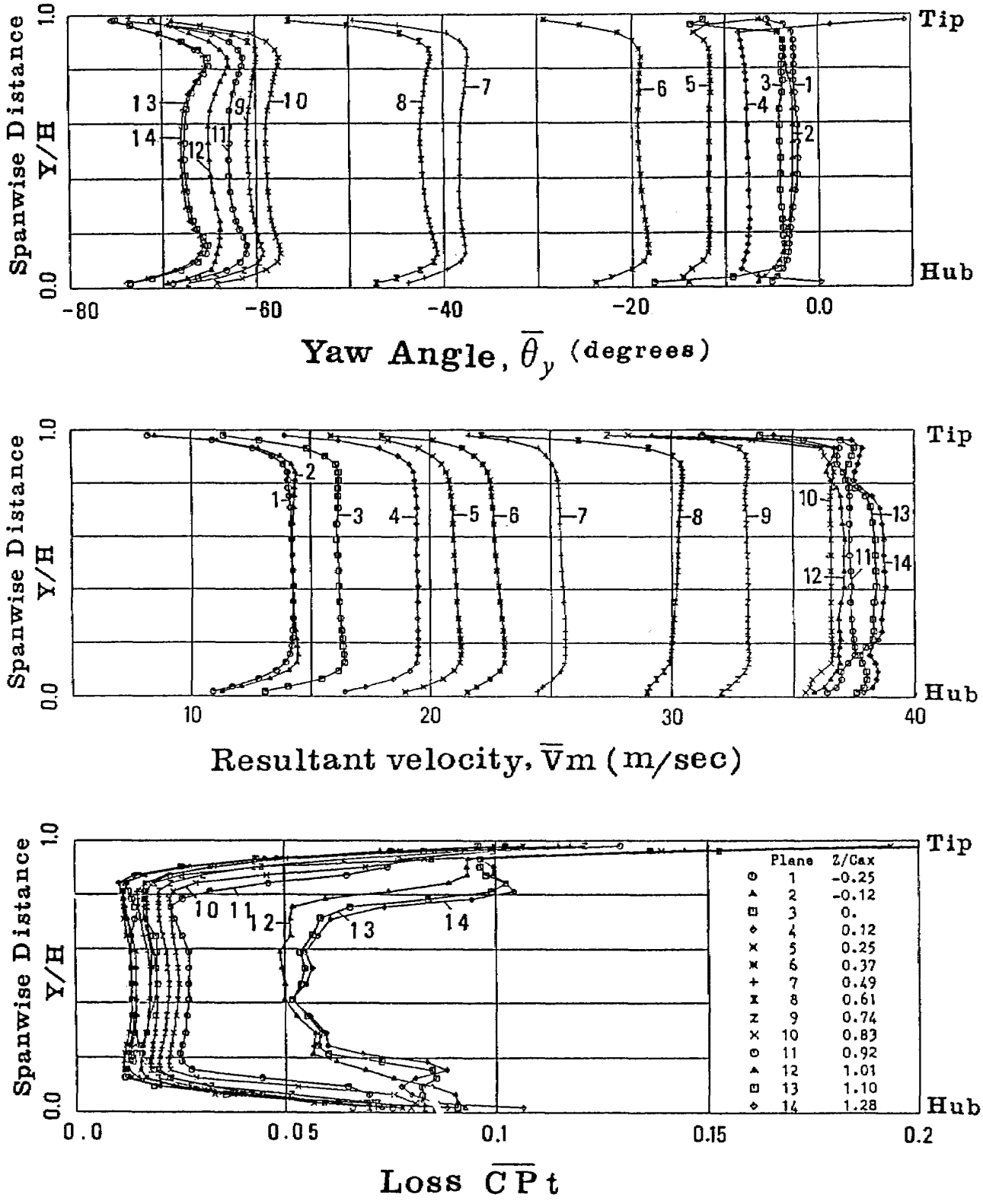

Fig. 6 Spanwise distribution of pitchwise-averaged yaw flow angle, resultant velocity, and total pressure loss coefficient

Evolution of Overall Total Pressure Loss through Stator Cascade (Fig. 7)

Fig. 7 presents serial color graphics of the loss development through the present stator cascade, and evolutions of the mass-averaged overall loss and of the loss obtained at the midspan location. The latter might correspond roughly to the cascade profile loss if loss migration from the endwall to the midspan were small. The difference between the overall loss and the midspan loss may be considered to be roughly equal to the secondary loss, including the inlet endwall boundary layer loss.

The loss in the present cascade shows little growth up to about Z/C_{ax} = 0.74 (plane 9) but rapidly increases from there to the trailing edge. Plane 9 corresponds to a plane at which the rolling-up of the low-energy fluids onto the SS

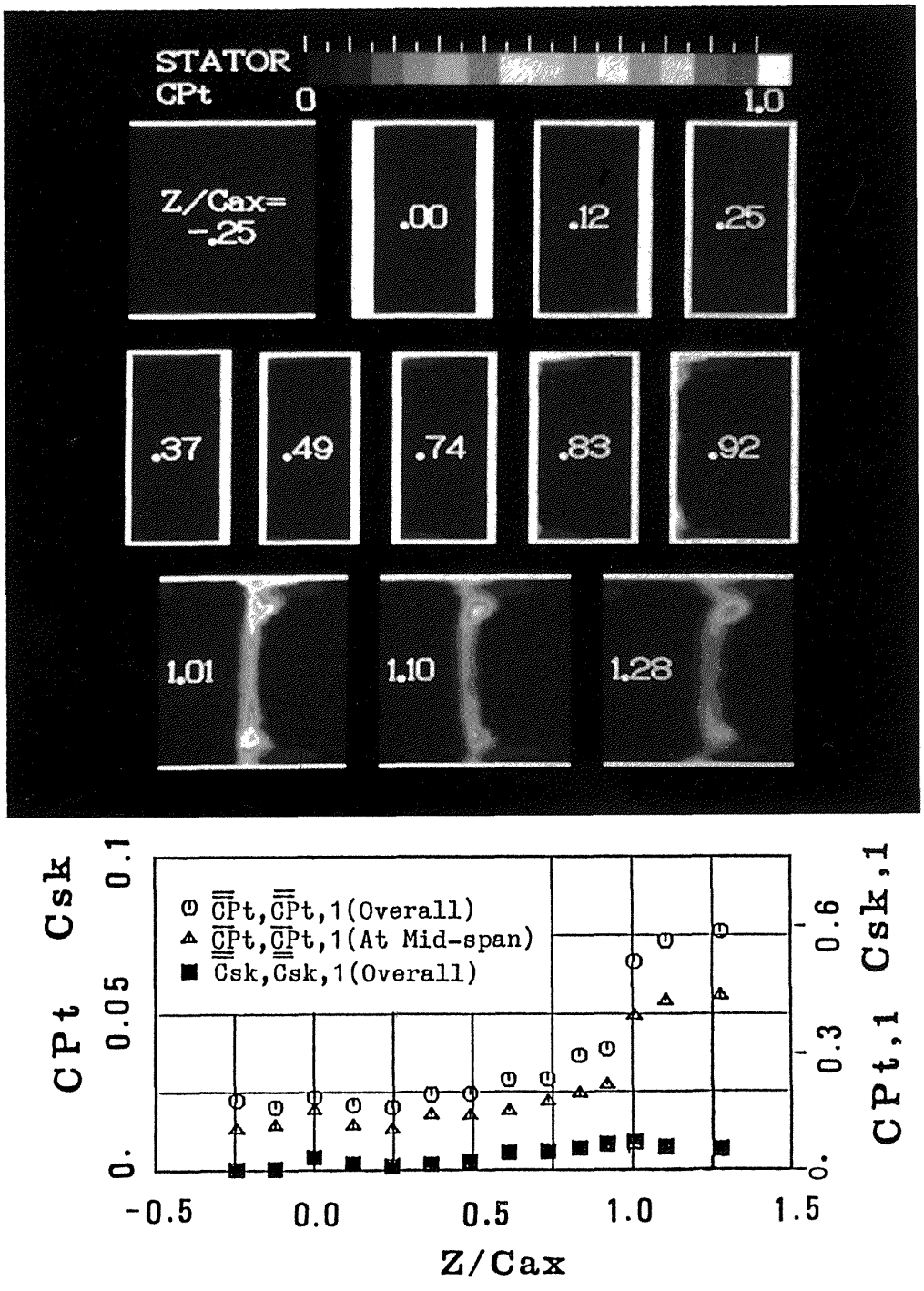

Fig. 7 Evolution of mass-averaged total pressure loss (straight stator cascade)

starts.

The secondary kinetic energy coefficients are also included in the same figure and they grow a little at the cascade inlet and between Z/C_{ax} = 0.5 and Z/C_{ax} = 1.0.

Downstream from the cascade, the growth rates of both overall loss and the midspan loss decrease. The value of the secondary kinetic energy also decreases.

CONCLUSIONS

The present study gave fairly detailed experiment data of secondary flows and losses in a straight stator cascade in order to estimate the loss mechanism quantitatively. A weak counter-vortex, the suction-side leg of the leading-edge horseshoe vortex, appeared at the suction surface/endwall corner in the upstream region of the present cascade but had no significant effects on the loss value. There was a high-loss region on the endwall near the pressure side of the cascade inlet region within the cascade, probably caused by the pressure-side leg of the leading-edge horseshoe vortex. This also did not affect the overall loss to any recognizable extent. Most of the loss produced within the cascade was due to the interaction of passage vortices with the suction surface downstream from the cascade throat.

ACKNOWLEDGMENTS

The authors wish to sincerely thank Mr. H. Tateishi, a staff member of Maruwa Electric Industry, for his assistance in the experimental work while he was working as a trainee at NAL for one year (April 1984-March 1985). The financial support provided by the Ministry of International Trade and Industry as a part of the national project for development of a high efficiency gas turbine is gratefully acknowledged.

REFERENCES

1) Sieverding, C.H., "Recent Progress in the Understanding of Basic Aspects of Secondary Flows in Turbine Blade Passages", ASME Journal of Gas Turbines and Power, Vol. 107, 1985, pp. 248-257.

2) Langston, L.S., Nice, M.L., and Hooper, R.M., "Three Dimensional Flow within a Turbine Cascade Passage", ASME Journal of Engineering for Power, Vol. 99, 1977, pp. 21-28.

3) Gregory-Smith, D.G., and Graves, C.P., "Secondary Flows and Losses in a Turbine Cascade", in: Viscous Effects in Turbomachines, AGARD-CP-351, 1983.

4) Sieverding, C.H., and Wilputte, Ph., "Influence of Mach Number and Endwall Cooling on Secondary Flows in a Straight Nozzle Cascade", ASME Journal of Engineering for Power, Vol. 103, 1981, pp. 257-264.

5) Marchal, P., and Sieverding, C.H., "Secondary Flows within Turbomachinery Bladings," in: Secondary Flows in Turbomachines, AGARD-CP-214, 1977.

6) Sieverding, C.H., Van How, W., and Boletis, E., "Experimental Study of the Three-Dimensional Flow Field in an Annular Turbine Nozzle Guidevane", ASME Journal of Gas Turbines and Power, Vol. 106, 1984, pp. 437-448.

7) Boletis, E., Sieverding, C.H., and Van Hove, W., "Effects of Skewed Inlet End Wall Boundary Layer on the 3-Dimensional Flow Field in an Annular Turbine Cascade", in: Viscous Effects in Turbomachines, AGARD-CP-351, 1983.

8) Boletis, E., "Effects of Tip Endwall Contouring on the Three Dimensional Flow Field in an Annular Turbine Nozzle Guide Vane: Part 1-Experimental Investigation", ASME Journal of Gas Turbines and Power, Vol. 107, 1985, pp. 983-990.

9) Yamamoto, A., and Yanagi, R., "Production and Development of Secondary Flows and Losses Within a Three Dimensional Turbine Stator Cascade", International Journal of Turbo and Jet-Engines, Vol. 3, No. 1, 1986, pp. 79-90.

10) Yamamoto, A., Takahara, K., Nouse, H., Inoue, S., Usui, H., and Mimura, F., "An Aerodynamic Design and the Overall Stage Performance of an Air-Cooled Axial-Flow Turbine", National Aerospace Laboratory, TR-321T, Jan. 1981.

11) Wu, C.H., "A General Theory of Three-Dimensional Flows in Subsonic and Supersonic Turbomachines of Axial-, Radial-, and Mixed-Flow Types", NACA 2604, 1952.

12) Hah, C., "A Navier-Stokes Analysis of Three-Dimensional Turbulent Flows inside Turbine Blade Rows at Design and Off-Design Conditions", ASME Journal of Gas Turbines and Power, Vol. 106, 1984, pp. 421-429.

13) Moore, J., and Adhye, R.Y., "Secondary Flows and Losses Downstream of a Turbine Cascade", ASME Journal of Gas Turbine and Power, Vol. 107, 1985, pp. 961-968.

14) Sjolander, S.A., "The Endwall Boundary Layer in an Annular Cascade of Turbine Nozzle Guide Vanes", Carleton U., TR ME/A 75-4, 1975.

15) Carrick, H.B., "Secondary Flow and Losses in Turbine Cascade With Inlet Skew", in: Secondary Flows in Turbomachines, AGARD-CP-214, 1977.

16) Moore, J. and Ransmayr, A., "Flow in a Turbine Cascade, Part 1: Losses and Leading-Edge Effects", ASME Journal of Gas Turbines and Power, Vol. 106, 1984, pp. 400-408.

17) Moore, J. and Smith, B.L., "Flow in a Turbine Cascade, Part 2: Measurement of Flow Trajectories by Ethylene Detection", ASME Journal of Gas Turbines and Power, Vol. 106, 1984, pp. 409-413.

18) Graziani, R.A., Blair, M.F., Taylor, J.R., and Mayle, R.E., "An Experimental Study of Endwall and Airfoil Surface Heat Transfer in a Large Scale Turbine Blade Cascade", ASME Paper No. 79-GT-99, 1979.

19) Yamamoto, A., Usui, H., and Mimura, F., "Secondary Flows and Losses in Two Types of Straight Turbine Cascades: Part 2-A Rotor Case", NAL TRT-975, 1988.

APPENDIX

Blade Profile Coordinates (Fig. 8)

The blade profile coordinates are given in Fig. 8 with the geometry drawing. The coordinate points were connected smoothly to make the blade profile.

No.	X_p	Y_p
1	7.76334	59.52613
2	11.82100	57.99053
3	15.72786	56.97294
4	19.14019	55.90000
5	22.52583	54.65911
6	26.02044	53.23361
7	30.38414	51.64429
8	35.05611	49.36351
9	39.87639	46.09354
10	45.52806	42.06619
11	50.75377	37.20366
12	56.10195	31.12360
13	61.49496	24.27752
14	67.03288	16.62206
15	72.82111	7.94290
16	78.29537	−0.65976

No.	X_s	Y_s
1	5.85767	73.00000
2	10.78546	74.76353
3	16.67151	75.80644
4	22.46210	75.68189
5	28.93445	75.09995
6	35.34520	73.09286
7	41.85698	69.25402
8	47.68002	64.49333
9	53.08374	59.07783
10	57.86537	52.29852
11	62.17482	45.48820
12	66.55599	37.85230
13	70.62326	29.57027
14	74.44284	20.53422
15	78.15102	10.52428
16	81.28619	0.68915

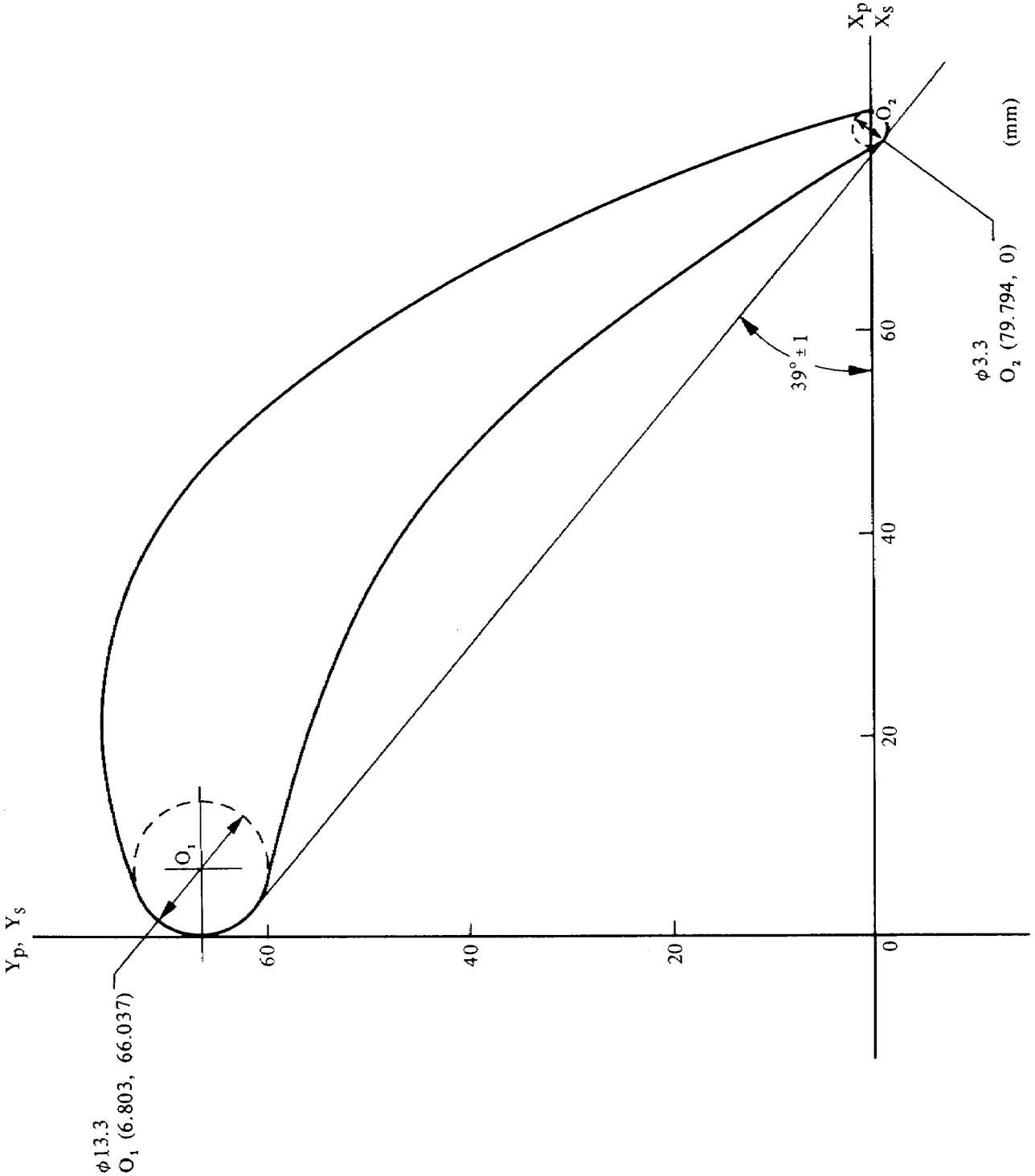

Fig. 8 Stator blade geometry

TECHNICAL REPORT OF NATIONAL
AEROSPACE LABORATORY
TR-974T

航空宇宙技術研究所報告974T号（欧文）

昭和63年5月発行

発行所　航空宇宙技術研究所
東京都調布市深大寺東町7丁目44番地1
電話三鷹 (0422) 47-5911（大代表）〒182
印刷所　株式会社　東京プレス
東京都板橋区桜川2－27－12

Published by
NATIONAL AEROSPACE LABORATORY
1,880 Jindaiji, Chōfu, Tokyo
JAPAN

Printed in Japan